A protein-DNA surface hydrogel mechanically reinforces the cell nucleus and protects the genome

Ramesh Adakkattil[†1], Pranay Mandal[†1-3], Yahor Savich[†1-3], Valentin Ruffine[4], Mareike A. Jordan[1], Henrik Dahl Pinholt[5], Elisabeth Fischer Friedrich[4], Frank Jülicher[*2,3,4], Stephan W Grill[*1,3,4], Alexander von Appen[*1,4]

[1]Max Planck Institute of Molecular Cell Biology and Genetics; Pfotenhauerstraße 108, 01307 Dresden, Germany.

[2]Max Planck Institute for the Physics of Complex Systems; Dresden 01187, Germany.

[3]Center for Systems Biology Dresden; 01062 Dresden, Germany.

[4]Cluster of Excellence Physics of Life, Technische Universität Dresden; 01062 Dresden, Germany.

[5]Institute for Medical Engineering and Science, Massachusetts Institute of Technology; Cambridge, MA, USA.

*Corresponding authors. Email: julicher@pks.mpg.de (F.J.); grill@mpi-cbg.de (S.W.G.); vonappen@mpi-cbg.de (A.v.A)

[†]These authors contributed equally to this work.

Abstract

The nuclear envelope protects the genome from mechanical stress during processes such as migration, division, and compression[1–6], but how it buffers forces at the scale of DNA remains unclear. Here, we utilize optical tweezers to show that a multivalent protein–DNA co-condensate containing the nuclear envelope protein LEM2[7,8] and the DNA-binding protein BAF [9,10] shield DNA beyond its melting point at 65 pN[11]. Under load, their collective assembly induces an unconventional DNA stiffening effect that provides mechanical reinforcement, dependent on the intrinsically disordered region (IDR) of LEM2. At the nuclear surface, these components form an elastic surface hydrogel in which LEM2 IDR-IDR interactions contract the surface hydrogel relative to its relaxed state, introducing a pre-stress in the lamin network. Inside cells, this surface hydrogel model can recapitulate elastic properties of the nuclear envelope measured via AFM indentation experiments as well as nuclear morphology, using parameters obtained at the molecular scale by use of optical tweezers. Disruption of the surface hydrogel increases DNA damage and micronuclei formation during nuclear deformation. These findings reveal a load-bearing, mesoscale surface hydrogel that reinforces the nucleus and expands the functional repertoire of biomolecular condensates to include DNA protection under mechanical stress.

Main Text

Mechanical stress can lead to DNA damage, such as double-strand breaks or micronucleation (Extended Data Fig.1a), which are associated with aging-related diseases including cancer, cardiomyopathies, and neurodegeneration[12–18]. The nuclear envelope is a mechanical scaffold that safeguards the genome[5], but how it protects the genome from mechanical stress-induced DNA damage is not well understood. The nuclear envelope is formed by a highly cross-linked network primarily composed of polymeric lamins, the outer and inner nuclear membranes (INM), and proteins that link the membrane to the encapsulated DNA[5]. Here, we focus our attention on BAF-LEM2, both essential for nuclear envelope reassembly and genome stability[6–9], that directly connects chromatin to the inner nuclear membrane[19–25]. Understanding how DNA is organized by BAF and the membrane-anchored LEM proteins, such as LEM2, function together can shed light on fundamental principles of nuclear functions and architecture. Notably, LEM2, along with other inner nuclear membrane proteins, contain substantial intrinsically disordered regions (IDRs) that protrude into the nucleoplasm, accounting for an estimated 30% of the total protein mass at the inner nuclear membrane (Fig. 1a, Extended Data Fig.1b, Extended Data Table 1). Proteins with extended IDRs can undergo phase separation to form biomolecular condensates[26,27] and even hydrogels[28,29]. LEM2 undergoes phase separation[7] to orchestrate nuclear membrane assembly during mitosis, driven by its amino-terminal IDR ($LEM2_{NTD}$). Recent evidence suggests that protein-DNA co-condensation can generate forces that contribute to biomolecular organization[30–32]. Hence, we here set out to investigate potential protective functions of an extended IDR meshwork built by phase separating proteins at the nuclear surface.

Protective DNA-protein co-condensation

We first set out to study the effects of BAF and LEM2 on DNA, and investigate the mechanical properties by use of optical tweezers. We established a minimal reconstitution system from

purified components (full-length BAF and the N-terminal domain of LEM2 containing the IDR but lacking the transmembrane domain; Fig. 1a, Extended Data Fig.1c-f) and tested if bulk phase separation can be observed, consistent with previous observation[7] (Extended Data Fig.1k). We found that phase separated LEM2 droplets enrich BAF and DNA *in vitro* (Fig. 1b, Extended Data Fig.1g). Since DNA, BAF and LEM2 enrich at the nuclear periphery in cells (Fig. 1c, Extended Data Fig.1h-j), it is possible that liquid-liquid phase separation and protein-DNA co-condensation contributes to the organization of the nuclear periphery.

We next set out to understand how BAF and LEM2 interact with individual DNA polymers. To this end, we added fluorescently labelled BAF and LEM2 to individual molecules of DNA stretched in the optical tweezer (methods, Extended Data Fig.2a,b) and followed the association of both proteins to DNA (Fig. 1d, Extended Data Fig.2d, Supplementary Video 1,2). We find that BAF homogeneously coats DNA in an apparently sequence-independent manner[33]. While we did not observe binding for LEM2 alone (500 nM; Fig. 1d, Supplementary Video 3), DNA-BAF caused instant LEM2 recruitment into a homogenous film. We conclude that BAF recruits LEM2[7] to DNA at physiologically relevant concentrations.

Given that LEM2 can undergo phase separation in bulk[7], we next set out to investigate if BAF-LEM2 can co-condense together with DNA[31]. We first focused on BAF alone, and used the optical tweezer to stretch a single molecule of λ-DNA to 16.7 µm end-to-end-distance (corresponding to ~40 pN of DNA tension, methods). We next allowed BAF to bind, and then gradually reduced DNA end-to-end distance. In all cases we observed that DNA tension reduces in the process, but plateaus at an average of 3.3±0.8 pN (Fig. 1e, Extended Data Fig.2f,g, methods) despite further reduction of the end-to-end distance. The occurrence of a constant tension plateau is indicative of a collective phase transition towards DNA-BAF co-condensate formation, similar to a 'sticky polymer' undergoing a globular collapse[31] (Fig. 1f, Extended Data Fig.2e, Supplementary Video 4). We measured the associated bulk condensation energy to be 0.2±0.1 k_BT/bp (methods, Fig. 1g, Extended Data Fig.2j,k,n). Adding 500nM LEM2, significantly below the saturation concentration[34] of LEM2 for bulk phase separation (4.0 µM, Extended Data Fig.1k,l), results in co-condensate formation at significantly increased plateau tension and with significantly increased bulk condensation energy (4.9±0.6 pN and 0.4±.02 k_BT/bp, respectively; Fig. 1e-g, Extended Data Fig.2h, Extended Data Fig.2l-n, methods, Supplementary Video 5). Instead, adding a variant of LEM2 that is unable to undergo bulk phase separation but still binds BAF ($LEM2_{MUT}$, Extended Data Fig.1f) results in only a marginal increase of both plateau tension and bulk condensation energy (4.1±0.5 pN and 0.3±.02 k_BT/bp, respectively; Fig. 1e,g). Taken together, DNA cross-bridging by BAF dimers alone can result in protein-DNA co-condensation. LEM2 stabilizes the DNA-BAF interaction, with a significant increase of the per basepair bulk co-condensation energy to a value that is ~20% of typical DNA basepair stacking energies[35]. We conclude that BAF-LEM2 can co-condense together with DNA.

Given that the bulk co-condensation energy is significant, one might expect DNA-BAF-LEM2 co-condensates to be stable and protect DNA from force-induced damage. To evaluate this possibility, we set out to unravel the co-condensates by force while investigating DNA integrity. We first focused on BAF alone. After forming a DNA-BAF co-condensate as described above, we gradually increased the end-to-end distance of DNA and recorded the tension applied (Fig. 1h,i;

methods). In all cases we observed that DNA tension increases in the process, to an average disassembly tension of 34±9 pN as the co-condensate unravels through many consecutive 'ripping events' each releasing extended amounts of DNA (Fig. 1h; methods, disassembly tension is independent of pulling speeds for speeds between 250 nm/s and 10 nm/s, Extended Data Fig.3a). We note that co-condensate disassembly tension is higher than the tension that needs to be applied to mechanically evict nucleosomes from DNA[36,37], indicative of strong DNA-BAF interactions. Concurrently, we measured the associated co-condensate disassembly work to be 2.3±0.7 k_BT/bp (Fig. 1k). Notably, the disassembly work of DNA-BAF-LEM2$_{MUT}$ co-condensates is not significantly increased as compared to DNA-BAF co-condensates (2.6±0.6 k_BT/bp, Extended Data Fig.3e,f). However, adding the phase-separating variant of LEM2 results in significantly increased DNA-BAF-LEM2 co-condensate disassembly tension and disassembly work (47±8 pN and 3.9±0.8 k_BT/bp, respectively; Fig. 1i,k), as well as a less pronounced 'rip pattern' (Fig. 1h). Remarkably, in all experiments involving BAF-LEM2, tension during unraveling surpasses the critical tension of 65 pN[11] required to melt DNA. Hence, we find that 66±22% of the DNA remains localized within the co-condensate when the melting tension of 65 pN is crossed for the first time, compared to 8±13% for DNA-BAF co-condensates (Fig. 1j). We conclude that, generally, disassembly tension during co-condensate unraveling is more than ~10x larger than plateau tension during co-condensate formation, and the per-base pair disassembly work is ~10x larger than the per-base pair bulk condensation energy (Fig. 1e,g,i,k). Such hysteresis arises when systems are unable to equilibrate on the experimental timescale (Extended Data Fig.3b-d; methods) particularly when kinetic barriers during formation and dissolution are different, and is often seen in systems that undergo a mesoscale phase transition[38]. Taken together, BAF-LEM2-DNA co-condensates are stable gel-like structures that can retain DNA when subjected to external forces larger than those required to melt DNA.

Is the DNA inside these co-condensates mechanically protected? We hypothesize that, in analogy to hydrogels in material science[39], cross-bridges and multivalent interactions formed by the IDRs of LEM2 function to redistribute mechanical tension, effectively lowering the tension that is experienced by DNA (Fig. 1n). To test if DNA tension inside DNA-BAF-LEM2 co-condensate is lower than DNA tension outside, we applied the tension-sensitive intercalating DNA dye Sytox Orange[40] (SO, methods). We find that at high external tension (52 pN), the intensity of SO is significantly higher outside the co-condensates (Fig. 1l, Extended Data Fig.3g,h; methods) than inside, consistent with DNA experiencing lower tension inside co-condensates as compared to outside. Furthermore, addition of the single-stranded DNA (ssDNA) sensor, FUS[31,41](Extended Data Fig.3i-k), reveals that at tensions up to ~85pN, DNA only melts outside the co-condensate and not inside (Fig. 1m, methods, Supplementary Video 6). We conclude that external tensions that are applied to DNA-BAF-LEM2 co-condensates likely percolate and redistribute throughout this gel-like structure, leading to an overall reduction of DNA tension inside. Therefore, protein-DNA co-condensates formed with multivalent protein-protein interactions can protect DNA from force-induced melting.

A reinforcing mechanical response

Multiple studies have reported that when cell nuclei are mechanically deformed and undergo nuclear blebbing, rupture, or micronucleation, BAF and LEM2 rapidly associate to DNA that is

143 mechanically stressed, exposed, or even expelled to the cytoplasm, likely to revert the
144 damage[9,12,23,24,42,43]. We therefore wondered if the *de-novo* assembly process of the BAF-LEM2
145 module on naked, mechanically stressed DNA imparts a more active role in protecting DNA. To
146 mimic such a re-assembly scenario under mechanical stress, we again stretched a single molecule
147 of λ-DNA to 16.7 µm end-to-end-distance (corresponding to ~40 pN of DNA tension), but now
148 monitored changes in DNA tension (by a value ΔT) during module assembly in a constant trap
149 position protocol (methods). Notably, we observed that in the first 100 seconds after addition of
150 BAF-LEM2, the beads in both optical traps are pulled inwards, due to a pulling tension generated
151 by the module assembly process that opposes the external tension applied by the two traps (Fig.
152 2a). This resulted in a DNA tension increase by ΔT = 7.5±0.9 pN, despite the high initial DNA
153 tension of 40 pN (Fig. 2b, methods). We note that neither the addition of BAF alone, nor adding
154 BAF together with the $LEM2_{MUT}$ resulted in a significant tension increase (Fig. 2b, ΔT = -0.2±0.9
155 pN for BAF; ΔT = 1.8±0.7 pN for BAF-$LEM2_{MUT}$). Finally, we find that ΔT increases with
156 increasing LEM2 concentration, and that, remarkably, ΔT increases in an apparently linear fashion
157 with initial DNA tension (Fig. 2c). The module thus displays features of a reinforcing response:
158 the higher the mechanical load on DNA, the more this module pulls back while re-assembling.

159 We next set out to shed light on the mechanism that underlies this reinforcing response. The linear
160 dependence of tension increase ΔT on initial tension suggests that LEM2 and its IDR interactions
161 introduce an additional compliant element. We therefore set out to determine the compliant
162 properties (i.e. effective stiffness and rest length, Extended Data Fig. 4a) of the combined DNA-
163 BAF-LEM2 module in comparison to naked DNA alone. We applied an initial tension between 20
164 and 40 pN, added BAF and LEM2, and then gradually increased extension while recording tension
165 to measure the effective stiffness of the entire assembly (Fig. 2d, Extended Data Fig.4b). We find
166 a linear relationship in the regime between 20 - 45 pN, with an effective stiffness ~1.3±0.1 fold
167 higher than for naked DNA (assuming saturation, K_0+K_i = 67±3 pN/µm; compared to K_0 = 51±2
168 pN/µm, Fig. 2d). Notably, the effective stiffness increases in a saturating manner with increasing
169 LEM2 concentration (Fig. 2e, Extended Data Fig.4f). We obtained an effective rest length by
170 extrapolating the linear fit to vanishing tension (Fig. 2d, Extended Data Fig. 4b,c; methods), and
171 found no significant difference between the two conditions (15.84±0.02 µm without BAF-LEM2
172 module, compared to 15.84±.01 µm with BAF-LEM2 module). Together, these results suggest a
173 picture where LEM2 IDR-IDR interactions generate compliant elements of identical rest length
174 assembled in parallel to DNA (Fig. 2f). We capture this mechanism in a theoretical description
175 that considers DNA mechanics in the enthalpic regime together with module assembly energetics
176 (stiffening reinforcement model, Supplementary Note 1): DNA is described as a chain of spring
177 elements, and the assembly of BAF-LEM2 modules results in the inclusion of additional spring
178 element in parallel and without a rest length change (Supplementary Note 1, methods, Extended
179 Data Fig. 4c-f). This description accounts for the dependence of stiffness on concentration (Fig.
180 2e, Extended Data Fig.4e,f) as well as the measured dependencies of ΔT on initial tension and
181 LEM2 concentration. We note that assembling compliant elements in parallel generates a
182 reinforcing response, as can be seen in Fig. 2d when keeping the end-to-end distance fixed: the
183 higher the initial tension, the higher the tension increase upon module assembly (red arrows). This
184 reveals a previously undescribed protein-induced reinforcing response, which, if operating at the
185 surface of the cell nucleus, would significantly impact cellular nuclear mechanics.

186 **The impact on nuclear surface mechanics**

187 We next set out to explore whether the reinforcing property of LEM2 manifests at the surface of
188 the nucleus in vivo (Fig. 1b,c; Extended Data Fig. 1h-j). To this end, we examined the morphology
189 of the protein–DNA interface at the INM in cryo-electron tomograms of focused ion beam milled
190 cellular thin sections. Across datasets from different cell types[44–46], we consistently observed an
191 amorphous, ~14 nm thick layer directly beneath the INM (Extended Data Fig. 5a-e). Notably, we
192 find that this layer excludes nucleosomes, revealing a nucleosome exclusion zone at the INM. In
193 agreement with previous studies, this region contains lamins[47–49] (Extended Data Fig. 5c,d). While
194 DNA cannot be directly visualized in these tomograms, independent work suggests that this layer
195 is enriched in DNA[50]. Given its position and composition, the zone includes BAF and the
196 transmembrane protein LEM2[51–53]. These findings support the existence of a gel-like, chromatin-
197 enveloping layer at the INM that potentially contributes to the mechanical reinforcement of the
198 nuclear surface (Fig. 1b,c; Extended Data Fig. 1h–j).

199 We next investigated if a) the material properties of this layer at the nuclear surface and thereby
200 b) nuclear morphology are affected when the LEM2-dependent reinforcing response is impaired.
201 We first evaluated if the effective area elastic modulus of the nuclear surface of the cells is changed
202 when LEM2 amounts are reduced by ~74% (from 8.2×10^4 to 2.1×10^4 molecules per cell,
203 Extended Data Fig. 6c-e, methods) using RNAi (siLEM2) , by using an AFM in conjunction with
204 confocal imaging (Fig. 3a,b, Extended Data Fig. 10e-g) to quantify the mechanical work (Fig. 3c)
205 associated with an increase of nuclear surface area (Extended Data Fig. 10b, methods). To probe
206 nuclear surface properties, we indented nuclei close to the plasma membrane of latrunculin-A
207 treated cells using an AFM (Extended Data Fig. 10a, methods) cantilever, and find that LEM2
208 depletion led to a $19.6 \pm 9.2\%$ reduction in the area elastic modulus (from 1.84 ± 0.15 pN/nm to
209 1.48 ± 0.12 pN/nm; Fig. 3d). We next evaluated if nuclear morphology is changed when LEM2
210 amounts are reduced (Fig.3e, Extended Data Fig. 6f-h). We find that reducing LEM2 amounts by
211 ~74% (methods) leads to a $5.4 \pm 2.0\%$ increase of nuclear surface area (from 516±6 μm^2 to 544±8
212 μm^2, Extended Data Fig. 6i,j) and a $28.6 \pm 8.0\%$ increase in nuclear asphericity (from
213 0.0700±0.0020 to 0.0903±0.0054, Fig. 3f bottom; asphericity defined as $A/A_V - 1$, where A_V is
214 the surface area of a sphere with equivalent nuclear volume). We note that we obtain qualitatively
215 similar results when impairing the LEM2-dependent reinforcing response via BAF RNAi (siBAF,
216 Extended Data Fig. 6a,b, Extended Data Fig. 8) with more significant changes to both nuclear
217 asphericity and area elastic modulus as compared to the LEM2 RNAi condition (Extended Data
218 Fig. 8l, Extended Data Fig. 8c). We conclude that reducing either LEM2 or BAF amounts by RNAi
219 results in a significant reduction in the effective area elastic modulus of the nuclear surface as well
220 as a significant increase of nuclear asphericity.

221 **A nuclear surface hydrogel**

222 How can a ~14 nm thick surface layer at the nuclear periphery, reinforced by LEM2, influence the
223 mechanical properties of the entire nucleus at the cellular scale? To address this, we developed a
224 mechanical model of the nuclear surface (Extended Data Fig. 5f) as a thin hydrogel layer. This
225 model (Fig. 3g) quantitatively incorporates the DNA-stiffening effects observed in vitro (Fig. 2)
226 along with measurements of nuclear surface mechanics and morphology in cells. We describe the

227 nuclear envelope as a two-dimensional elastic surface hydrogel that encloses the nucleoplasm at
228 constant volume. In the absence of BAF-LEM2, the surface hydrogel is characterized by a bending
229 modulus (κ) and a bare area elastic modulus (λ). We capture the effect of the BAF-LEM2 module
230 by introducing a surface density of additional elastic spring elements (Supplementary Note 1, Eq.
231 19). The bare area elastic modulus λ is largely determined by the lamin network[54], and the elastic
232 springs have the reinforcing properties described above (Supplementary Note 1, Eq. 36). The effect
233 of an increase of nuclear asphericity upon BAF-LEM2 module impairment via LEM2 or BAF
234 depletion (Supplementary Note 1) can be accounted for if the elastic spring elements associated
235 with the BAF-LEM2 module contract the surface hydrogel relative to its relaxed state due to a
236 rest-length mismatch between the two systems, introducing a pre-stress. When LEM2 or BAF
237 levels are reduced, the elastic spring elements are removed and the surface hydrogel can relax,
238 increasing its surface area and leading to more aspherical shapes (Fig. 3f bottom, Extended Data
239 Fig. 6i,j, Extended Data Fig. 8j-l). We next used the AFM measurements (Fig. 3d, Extended Data
240 Fig. 8c, Extended Data Fig. 10c,d) as well as the reinforcing properties of the BAF-LEM2 module
241 characterized in the optical tweezer to quantitatively account for the observed nuclear shape
242 changes upon either LEM2 depletion (Fig. 3f, top) or BAF depletion (Extended Data Fig. 8l top,
243 Supplementary Note 1), using this REst-length Mismatched Multicomponent (REMM) surface
244 hydrogel model (Supplementary Note 1). We use the rest length mismatch, the relaxed surface
245 area as well as the bare area elastic modulus λ as parameters. Our analysis suggests that λ is ~25
246 times smaller than the effective area elastic moduli measured with the AFM in control cells. This
247 suggests a soft lamin network providing mainly entropic elasticity[55]. Because the lamin network
248 is soft, changing the stiffness of reinforcing BAF-LEM2 spring elements has a significant effect
249 on the material properties of the REMM surface hydrogel. This model can therefore account for
250 the observed changes in area elastic modulus and nuclear shape. We conclude that the REMM
251 surface hydrogel model, taking into account a stiffening effect based on LEM2 IDR-IDR
252 interactions characterized on the molecular scale, can capture nuclear surface properties at the
253 cellular scale.

254 We next asked if the LEM2 component of this surface hydrogel imparts specific protective
255 functions. We find that under compression (Extended Data Fig. 9a-b), cells depleted of LEM2 by
256 RNAi accumulate significantly higher levels of DNA double-strand breaks (Extended Data Fig.
257 9c,d,g-l) and display a larger degree of micronucleation (Extended Data Fig. 9e,f, Extended Data
258 Fig. 10h-k)[13,18]. We conclude that, consistent with our optical tweezer results and our expectations
259 from theory, the LEM2 component, with its IDR's, provides a specific protective function against
260 mechanically induced damage.

261 **Discussion**

262 Here, we have used optical tweezers and *in vitro* reconstitution to show that BAF and LEM2 form
263 multivalent protein–DNA co-condensates. We reveal that i) these multivalent assemblies shield
264 DNA beyond its melting threshold at 65 pN of tension, and ii) their assembly on DNA stretched
265 close to melting, generates forces that counteract the stretch. Notably, a surface hydrogel model
266 incorporating the second effect quantitatively recapitulates elastic properties of the nuclear
267 envelope at the cellular scale, using parameters obtained at the molecular scale by use of optical
268 tweezers. Our work paints a picture (Fig. 3g) where the inner nuclear membrane protein LEM2

and the DNA crosslinking factor BAF form a pre-stressed surface hydrogel together with the nuclear lamins that can dynamically resist mechanical stress applied to the nuclear periphery. This is achieved via a molecular reinforcing response based on LEM2's IDR-IDR interactions, converting up to ~0.25 K_BT of free energy per LEM2 molecule into mechanical work (methods). Given that there are no ATPases involved (Fig. 2), this free energy should derive from molecular-scale assembly processes but can impact large-scale nuclear organization and nuclear shape, thereby helping to preserve chromatin integrity (methods).

Together, this uncovers a novel design principle in which multivalent protein networks assemble on DNA polymers, generating reinforcement responses that buffer mechanical damage and enhance structural resilience; a strategy reminiscent of load-bearing tough hydrogels in material science[39,56]. Given the interconnected architecture of the inner nuclear membrane, this mechanism likely extends beyond BAF-LEM2 to include other LEM domain proteins[19], IDR-containing inner nuclear membrane proteins such as lamins or lamin B receptor[54,57,58], and even chromatin itself[9,51,59]. Lastly, the ability of DNA-protein co-condensation to generate biologically relevant forces suggests a broader dynamic role of condensates in shaping functional chromatin structures during processes such as transcription and replication[60–63].

References

1. Shah, P. *et al.* Nuclear deformation causes DNA damage by increasing replication stress. *Curr. Biol.* **31**, 753–765.e6 (2021).
2. Ganem, N. J. & Pellman, D. Linking abnormal mitosis to the acquisition of DNA damage. *J. Cell Biol.* **199**, 871–881 (2012).
3. Denais, C. M. *et al.* Nuclear envelope rupture and repair during cancer cell migration. *Science* **352**, 353–358 (2016).
4. Raab, M. *et al.* ESCRT III repairs nuclear envelope ruptures during cell migration to limit DNA damage and cell death. *Science* **352**, 359–362 (2016).
5. Ungricht, R. & Kutay, U. Mechanisms and functions of nuclear envelope remodelling. *Nat. Rev. Mol. Cell Biol.* **18**, 229–245 (2017).
6. LaJoie, D. & Ullman, K. S. Coordinated events of nuclear assembly. *Curr. Opin. Cell Biol.* **46**, 39–45 (2017).
7. von Appen, A. *et al.* LEM2 phase separation promotes ESCRT-mediated nuclear envelope reformation. *Nature* (2020) doi:10.1038/s41586-020-2232-x.
8. Gu, M. *et al.* LEM2 recruits CHMP7 for ESCRT-mediated nuclear envelope closure in fission yeast and human cells. *Proceedings of the National Academy of Sciences* **114**, E2166–E2175 (2017).
9. Samwer, M. *et al.* DNA Cross-Bridging Shapes a Single Nucleus from a Set of Mitotic Chromosomes. *Cell* (2017) doi:10.1016/j.cell.2017.07.038.
10. Skoko, D. *et al. Barrier-to-Autointegration Factor (BAF) Condenses DNA by Looping*.
11. van Mameren, J. *et al.* Unraveling the structure of DNA during overstretching by using multicolor, single-molecule fluorescence imaging. *Proc. Natl. Acad. Sci. U. S. A.* **106**,

308 18231–18236 (2009).
309 12. Liu, S. *et al.* Nuclear envelope assembly defects link mitotic errors to chromothripsis.
310 *Nature* Preprint at https://doi.org/10.1038/s41586-018-0534-z (2018).
311 13. Ross, J. A. *et al.* Lem2 is essential for cardiac development by maintaining nuclear integrity.
312 *Cardiovasc. Res.* **119**, 2074–2088 (2023).
313 14. Feurle, P. *et al.* SATB2-LEMD2 interaction links nuclear shape plasticity to regulation of
314 cognition-related genes. *EMBO J.* **40**, e103701 (2021).
315 15. Nava, M. M. *et al.* Heterochromatin-driven nuclear softening protects the genome against
316 mechanical stress-induced damage. *Cell* **181**, 800–817.e22 (2020).
317 16. Papathanasiou, S. *et al.* Heritable transcriptional defects from aberrations of nuclear
318 architecture. *Nature* **619**, 184–192 (2023).
319 17. Marbach, F. *et al.* The Discovery of a LEMD2-Associated Nuclear Envelopathy with Early
320 Progeroid Appearance Suggests Advanced Applications for AI-Driven Facial Phenotyping.
321 *Am. J. Hum. Genet.* **104**, 749–757 (2019).
322 18. Caravia, X. M. *et al.* Loss of function of the nuclear envelope protein LEMD2 causes DNA
323 damage-dependent cardiomyopathy. *J. Clin. Invest.* **132**, (2022).
324 19. Barton, L. J., Soshnev, A. A. & Geyer, P. K. Networking in the nucleus: A spotlight on
325 LEM-domain proteins. *Current Opinion in Cell Biology* Preprint at
326 https://doi.org/10.1016/j.ceb.2015.03.005 (2015).
327 20. Tapia, O., Fong, L. G., Huber, M. D., Young, S. G. & Gerace, L. Nuclear envelope protein
328 Lem2 is required for mouse development and regulates MAP and AKT kinases. *PLoS One*
329 **10**, e0116196 (2015).
330 21. Schirmer, E. C., Florens, L., Guan, T., Yates, J. R., 3rd & Gerace, L. Nuclear membrane
331 proteins with potential disease links found by subtractive proteomics. *Science* **301**, 1380–
332 1382 (2003).
333 22. Ulbert, S., Antonin, W., Platani, M. & Mattaj, I. W. The inner nuclear membrane protein
334 Lem2 is critical for normal nuclear envelope morphology. *FEBS Lett.* **580**, 6435–6441
335 (2006).
336 23. Halfmann, C. T. *et al.* Repair of nuclear ruptures requires barrier-to-autointegration factor. *J.*
337 *Cell Biol.* **218**, 2136–2149 (2019).
338 24. Young, A. M., Gunn, A. L. & Hatch, E. M. BAF facilitates interphase nuclear membrane
339 repair through recruitment of nuclear transmembrane proteins. *Mol. Biol. Cell* (2020)
340 doi:10.1091/mbc.E20-01-0009.
341 25. Webster, B. M. *et al.* Chm7 and Heh1 collaborate to link nuclear pore complex quality
342 control with nuclear envelope sealing. *EMBO J.* **35**, 2447–2467 (2016).
343 26. Brangwynne, C. P. *et al.* Germline P granules are liquid droplets that localize by controlled
344 dissolution/condensation. *Science* (2009) doi:10.1126/science.1172046.
345 27. Li, P. *et al.* Phase transitions in the assembly of multivalent signalling proteins. *Nature*
346 (2012) doi:10.1038/nature10879.

347 28. Frey, S., Richter, R. P. & Görlich, D. FG-rich repeats of nuclear pore proteins form a three-
348 dimensional meshwork with hydrogel-like properties. *Science* **314**, 815–817 (2006).
349 29. Kato, M. *et al.* Cell-free formation of RNA granules: low complexity sequence domains
350 form dynamic fibers within hydrogels. *Cell* **149**, 753–767 (2012).
351 30. Quail, T. *et al.* Force generation by protein–DNA co-condensation. *Nat. Phys.* (2021)
352 doi:10.1038/s41567-021-01285-1.
353 31. Renger, R. *et al.* Co-condensation of proteins with single- and double-stranded DNA. *Proc*
354 *Natl Acad Sci U S A* **119**, e2107871119 (2022).
355 32. Keenen, M. M. *et al.* HP1 proteins compact DNA into mechanically and positionally stable
356 phase separated domains. *Elife* **10**, (2021).
357 33. Zheng, R. *et al.* Barrier-to-autointegration factor (BAF) bridges DNA in a discrete, higher-
358 order nucleoprotein complex. *Proc Natl Acad Sci U S A* **97**, 8997–9002 (2000).
359 34. Fritsch, A. W., Iglesias-Artola, J. M. & Hyman, A. A. inPhase - A simple, accurate and fast
360 approach to determine phase diagrams of protein condensates. *bioRxiv* (2024)
361 doi:10.1101/2024.10.02.616352.
362 35. Delcourt, S. G. & Blake, R. D. Stacking energies in DNA. *J Biol Chem* **266**, 15160–15169
363 (1991).
364 36. Cui, Y. & Bustamante, C. Pulling a single chromatin fiber reveals the forces that maintain
365 its higher-order structure. *Proc Natl Acad Sci U S A* **97**, 127–132 (2000).
366 37. Mihardja, S., Spakowitz, A. J., Zhang, Y. & Bustamante, C. Effect of force on
367 mononucleosomal dynamics. *Proc Natl Acad Sci U S A* **103**, 15871–15876 (2006).
368 38. Jülicher, F. & Weber, C. A. Droplet Physics and Intracellular Phase Separation. *Annu. Rev.*
369 *Condens. Matter Phys.* **15**, 237–261 (2024).
370 39. Liu, C. *et al.* Tough hydrogels with rapid self-reinforcement. *Science* **372**, 1078–1081
371 (2021).
372 40. King, G. A., Biebricher, A. S., Heller, I., Peterman, E. J. G. & Wuite, G. J. L. Quantifying
373 local molecular tension using intercalated DNA fluorescence. *Nano Lett.* **18**, 2274–2281
374 (2018).
375 41. Ozdilek, B. A. *et al.* Intrinsically disordered RGG/RG domains mediate degenerate
376 specificity in RNA binding. *Nucleic Acids Res* **45**, 7984–7996 (2017).
377 42. Jung-Garcia, Y. *et al.* LAP1 supports nuclear adaptability during constrained melanoma cell
378 migration and invasion. *Nat Cell Biol* **25**, 108–119 (2023).
379 43. Vietri, M. *et al.* Unrestrained ESCRT-III drives micronuclear catastrophe and chromosome
380 fragmentation. *Nat. Cell Biol.* (2020) doi:10.1038/s41556-020-0537-5.
381 44. Taniguchi, R. *et al.* Nuclear pores safeguard the integrity of the nuclear envelope. *Nat. Cell*
382 *Biol.* **27**, 762–775 (2025).
383 45. Kreysing, J. P. *et al.* Passage of the HIV capsid cracks the nuclear pore. *Cell* **188**, 930–
384 943.e21 (2025).
385 46. Xing, H. *et al.* Translation dynamics in human cells visualized at high resolution reveal

386 cancer drug action. *Science* **381**, 70–75 (2023).
387 47. Turgay, Y. *et al.* The molecular architecture of lamins in somatic cells. *Nature* **543**, 261–264
388 (2017).
389 48. Wang, B. *et al.* The molecular basis of lamin-specific chromatin interactions. *Nat. Struct.*
390 *Mol. Biol.* (2025) doi:10.1038/s41594-025-01622-5.
391 49. Mahamid, J. *et al.* Visualizing the molecular sociology at the HeLa cell nuclear periphery.
392 *Science* **351**, 969–972 (2016).
393 50. Ou, H. D. *et al.* ChromEMT: Visualizing 3D chromatin structure and compaction in
394 interphase and mitotic cells. *Science* **357**, (2017).
395 51. Horikoshi, N. *et al.* Cryo-EM structures of the BAF-Lamin A/C complex bound to
396 nucleosomes. *Nat Commun* **16**, 1495 (2025).
397 52. Samson, C. *et al.* Structural analysis of the ternary complex between lamin A/C, BAF and
398 emerin identifies an interface disrupted in autosomal recessive progeroid diseases. *Nucleic*
399 *Acids Res.* **46**, 10460–10473 (2018).
400 53. Brachner, A., Reipert, S., Foisner, R. & Gotzmann, J. LEM2 is a novel MAN1-related inner
401 nuclear membrane protein associated with A-type lamins. *J. Cell Sci.* **118**, 5797–5810
402 (2005).
403 54. Dahl, K. N., Kahn, S. M., Wilson, K. L. & Discher, D. E. The nuclear envelope lamina
404 network has elasticity and a compressibility limit suggestive of a molecular shock absorber.
405 *J. Cell Sci.* **117**, 4779–4786 (2004).
406 55. Mostafazadeh, N. & Peng, Z. Microstructure-based nuclear lamina constitutive model.
407 *Cytoskeleton (Hoboken)* **81**, 297–309 (2024).
408 56. Petelinšek, N. & Mommer, S. Tough Hydrogels for Load-Bearing Applications. *Adv Sci*
409 *(Weinh)* **11**, e2307404 (2024).
410 57. Solovei, I. *et al.* LBR and lamin A/C sequentially tether peripheral heterochromatin and
411 inversely regulate differentiation. *Cell* **152**, 584–598 (2013).
412 58. Swift, J. *et al.* Nuclear Lamin-A Scales with Tissue Stiffness and Enhances Matrix-Directed
413 Differentiation. *Science* **341**, 1240104 (2013).
414 59. Sanulli, S. *et al.* HP1 reshapes nucleosome core to promote phase separation of
415 heterochromatin. *Nature* **575**, 390–394 (2019).
416 60. Zhang, M. *et al.* Lamin A/C safeguards replication initiation by orchestrating chromatin
417 accessibility and PCNA recruitment. *bioRxivorg* 2025.03.06.641818 (2025).
418 61. Cherdyntseva, V. *et al.* Nucleoplasmic Lamin A/C controls replication fork restart upon
419 stress by modulating local H3K9me3 and ADP-ribosylation levels. *bioRxivorg*
420 2025.01.18.633737 (2025).
421 62. Sidorenko, E. *et al.* Lamina-associated polypeptide 2α is required for intranuclear MRTF-A
422 activity. *Sci Rep* **12**, 2306 (2022).
423 63. Ferraioli, S. *et al.* LAP2alpha facilitates myogenic gene expression by preventing
424 nucleoplasmic lamin A/C from spreading to active chromatin regions. *Nucleic Acids Res* **52**,

11500–11518 (2024).
64. Cai, M. *et al.* Solution NMR structure of the barrier-to-autointegration factor-emerin complex. *J. Biol. Chem.* (2007) doi:10.1074/jbc.M700576200.
65. Bradley, C. M., Ronning, D. R., Ghirlando, R., Craigie, R. & Dyda, F. Structural basis for DNA bridging by barrier-to-autointegration factor. *Nat. Struct. Mol. Biol.* **12**, 935–936 (2005).
66. Jumper, J. *et al.* Highly accurate protein structure prediction with AlphaFold. *Nature* **596**, 583–589 (2021).
67. Pettersen, E. F. *et al.* UCSF ChimeraX: Structure visualization for researchers, educators, and developers. *Protein Sci.* **30**, 70–82 (2021).
68. Cho, N. H. *et al.* OpenCell: Endogenous tagging for the cartography of human cellular organization. *Science* **375**, eabi6983 (2022).
69. Spakman, D., King, G. A., Peterman, E. J. G. & Wuite, G. J. L. Constructing arrays of nucleosome positioning sequences using Gibson Assembly for single-molecule studies. *Sci Rep* **10**, 9903 (2020).
70. Aicart-Ramos, C., Hormeno, S., Wilkinson, O. J., Dillingham, M. S. & Moreno-Herrero, F. Long DNA constructs to study helicases and nucleic acid translocases using optical tweezers. *Methods Enzymol* **673**, 311–358 (2022).
71. Liu, Y.-T. *et al.* Isotropic reconstruction for electron tomography with deep learning. *Nat. Commun.* **13**, 6482 (2022).
72. Heebner, J. E. *et al.* Deep Learning-Based Segmentation of Cryo-Electron Tomograms. *J Vis Exp* (2022) doi:10.3791/64435.
73. Kremer, J. R., Mastronarde, D. N. & Mcintosh, J. R. Computer visualization of three-dimensional image data using IMOD J. *J. Struct. Biol* **116**, 71–76 (1996).

Acknowledgments

We thank Jose Alberto Morin for the initial experiments on this system with the optical tweezer. We thank Tony Hyman, Anatol Fritsch and Juan Iglesias for help with phase separation saturation concentration determination, and Martin Beck and Reiya Taniguchi for sharing cryo electron tomography data. We thank the staff and students of the 2023 MBL Physiology course where important theory, initial experiments but no controls were performed, particularly A. Ortega Granillo, J. Brzostowski, N.King, and D. Fletcher. We thank the following services and facilities at MPI-CBG Dresden for their support: Protein Expression Facility, Biophysics Core facility, Scientific Computing Facility, Genome Engineering Facility and the Light Microscopy Facility.

Funding

Funding by the Max Planck Society (AvA, SWG, FJ)

European Research Council-Organelloids 101117619 (AvA)

German Research Foundation SPP2191 (AvA)

Heineman Foundation through Minerva (AvA)

Volkswagen Foundation (FJ)

Competing interests

Authors declare that they have no competing interests.

Supplementary Information

Extended Data Figs. 1-10

Materials and Methods

Supplementary Note 1

Supplementary Note 2

Extended Data Table 1

Supplementary Video 1- 6

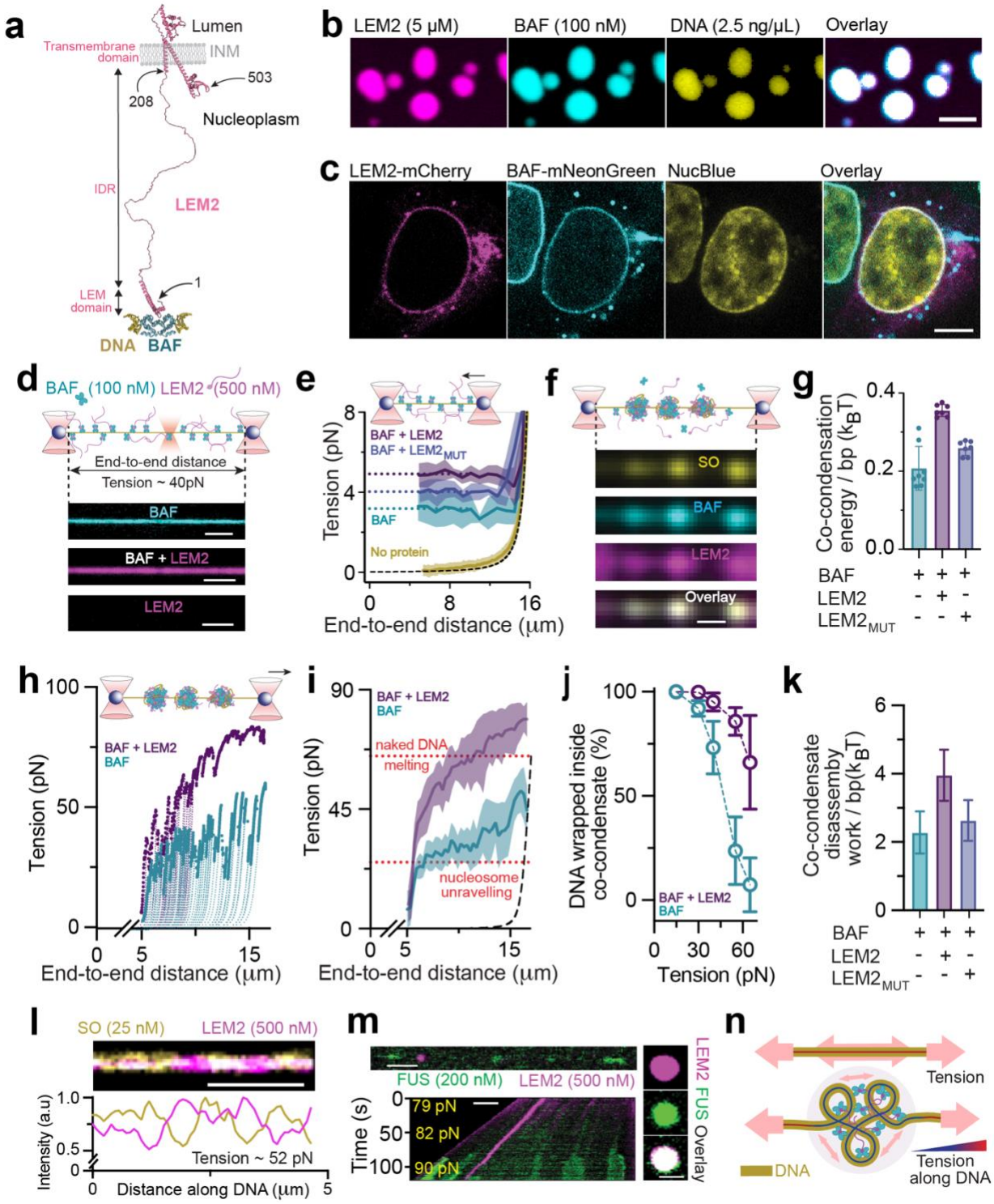

Fig. 1: Co-condensation with BAF-LEM2 shields DNA beyond the melting transition.

a, DNA-BAF-LEM2 interfaces the chromatin surface with the INM. Numbers indicate amino acid positions.

480 **b,** Confocal imaging reveals bulk phase separation of reconstituted DNA-BAF-LEM2 (methods).

481 **c,** Confocal imaging of BAF, LEM2 and DNA in the nucleus shows enrichment at the nuclear
482 envelope (methods).

483 **d,** Top, schematic of the optical tweezers assay where a single λ-DNA molecule is held between
484 two optically trapped beads (large red cones with spheres) via biotin-streptavidin interactions at a
485 tension of ~40 pN. Confocal imaging (small red cone) reveals BAF and LEM2 association to the
486 stretched DNA. Bottom, confocal images of BAF (top), BAF and LEM2 (middle) and LEM2
487 (bottom) association to stretched λ-DNA.

488 **e,** Average tension vs. end-to-end distance graphs obtained with the optical tweezer by gradually
489 reducing DNA end-to-end distance from 16.7 µm to 5 µm (top inset) reveals a constant tension
490 plateau indicative of protein-DNA co-condensation of DNA with BAF (n = 8), with
491 BAF+LEM2$_{MUT}$ (n = 7), and with BAF+LEM2 (n = 7; methods). Solid colored lines, average
492 tension; colored shaded regions, mean ± standard deviation; dotted lines, extrapolations of tension
493 to zero end-to-end distance; dashed black line, worm-like-chain (WLC) model of λ-DNA elasticity
494 (methods).

495 **f,** Schematic representation (top) and representative example from (**e**) (bottom) of DNA-BAF-
496 LEM2 co-condensates, DNA (yellow) is labelled with Sytox Orange (SO). Scale bar, 0.5 µm.

497 **g,** Co-condensation energy per DNA base pair (bp) obtained by integration of the tension vs.
498 distance curves in (e). Co-condensation energy is significantly higher for DNA-BAF-LEM2 than
499 for DNA-BAF and DNA-BAF-LEM2$_{MUT}$.

500 **h,** Representative tension vs. end-to-end distance graphs (solid dots) obtained by gradually
501 increasing DNA end-to-end distance from 5 µm to ~16.5 µm (top inset) reveals characteristic 'rip
502 patterns', with each rip unraveling extended amounts of DNA, during DNA-BAF and DNA-BAF-
503 LEM2 co-condensate tension-induced disassembly. Dotted lines, WLC fits (methods) reveal the
504 contour length of DNA inside co-condensates (see Fig. 1j).

505 **i,** Corresponding average tension vs. end-to-end distance graphs for DNA-BAF (n = 10), and
506 DNA-BAF-LEM2 (n = 10; methods) co-condensate tension-induced disassembly. Solid colored
507 lines, average tension; colored shaded regions, mean ± standard deviation. DNA-BAF co-
508 condensates disassemble at tensions slightly higher than those required to dissociate nucleosomes
509 from DNA, while disassembling DNA-BAF+LEM2 co-condensates requires tensions above the
510 critical melting tension of 65 pN. Dashed black line, WLC model of λ-DNA.

511 **j,** Fraction of DNA remaining co-condensed during tension-induced disassembly as a function of
512 applied tension. Note that 66±22 % of DNA remains co-condensed with BAF+LEM2 at the critical
513 melting tension of 65 pN.

514 **k,** Co-condensate per-base pair disassembly work obtained by integration of the tension vs.

515 distance curves in Fig. 1i (BAF and BAF-LEM2) and Extended data Fig. 3e,f (BAF-LEM2$_{MUT}$;
516 n=5).

517 **l,** Top, confocal image of SO, bright in directions of high DNA tension and dim in regions of low
518 DNA tension, at 52 pN DNA tension reveals that DNA tension is higher outside co-condensates
519 than inside. Bottom, corresponding profiles of normalized intensities showing alternate low and
520 high distributions.

521 **m,** Left, representative image (top) and kymograph (bottom) of DNA-BAF-LEM2 co-condensate
522 disassembly under high tension reveals that the ssDNA binding protein FUS (green) exclusively
523 associates with non-co-condensed regions, revealing that DNA inside co-condensates is protected
524 from melting. Right, FUS partitions into LEM2 condensates in bulk, indicating that FUS is not
525 excluded from DNA-BAF-LEM2 co-condensates.

526 **n,** Sketch of the IDR-dependent mechanism of co-condensate tension buffering. DNA tension
527 (pink arrows) is reduced within co-condensate (bottom) as compared to without (top), since inside
528 tension redistributes through IDR-IDR and other molecular interactions. Arrow thickness indicates
529 relative tension strength, and direction shows the path of redistribution. The color bar represents
530 tension magnitude along the DNA.

531 Scale bar, 5 μm in (**b,c**),(**m**)-right and 2 μm in (**d,l**), (**m**)-left**.**

532

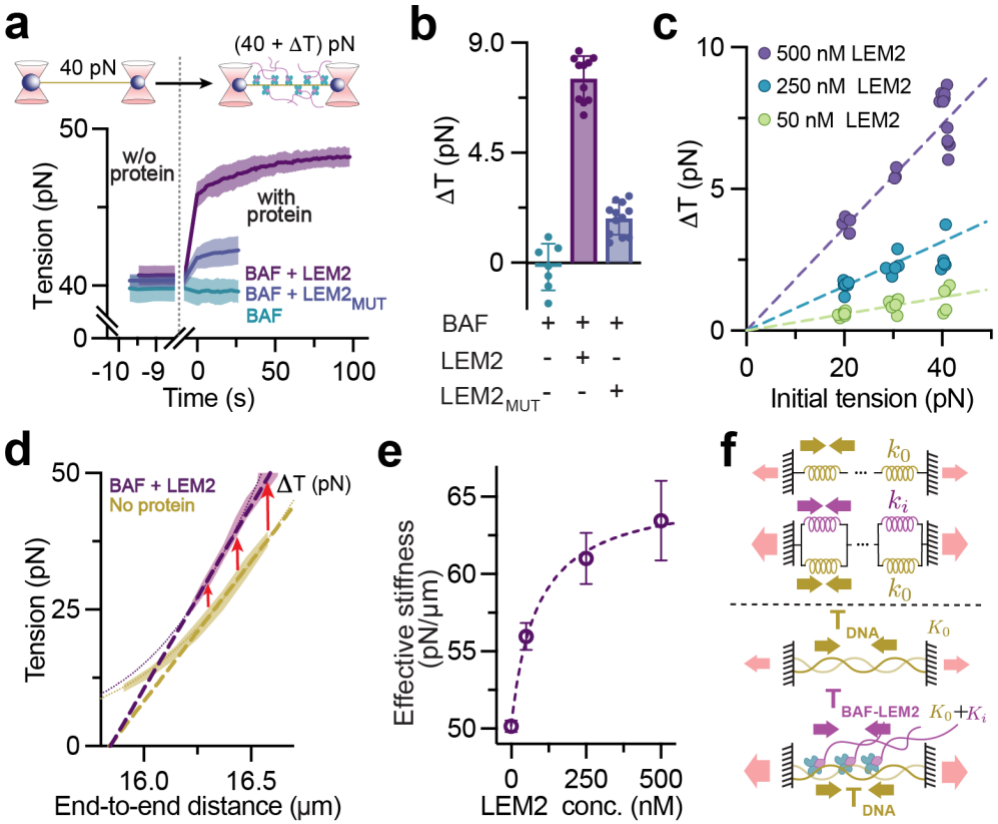

Fig. 2: BAF-LEM2 assembly on DNA generates a reinforcing response.

a, Top, DNA stretched to an initial ~40 pN tension is subjected to a buffer exchange from protein-free (left) to protein-containing (right) at time t = 0s while trap positions are maintained. Bottom, tension increases with time post addition of 100nM BAF + 500nM LEM2 (BAF+LEM2) and 100nM BAF + 500nM $LEM2_{MUT}$ (BAF+$LEM2_{MUT}$) due to module assembly on DNA, but does not increase post addition of 100nM BAF alone. Solid colored lines, mean tension; colored shaded regions, mean ± standard deviation (BAF: n=7, BAF-LEM2: n=11, BAF-$LEM2_{MUT}$: n=12).

b, Corresponding average tension increases ΔT.

c, ΔT as a function of initial DNA tension and LEM2 concentration (100nM BAF, n=20 for 500nM LEM2, n=17 for 250nM LEM2, : n=19 for 50nM LEM2). Dashed lines, linear fits.

d, Direct experimental characterization of BAF-LEM2 module compliance in the enthalpic regime of DNA stretching via average tension vs. DNA end-to-end distance graphs in absence (yellow shaded region, mean ± standard deviation, n=11) and in presence (magenta shaded region, mean ± standard deviation, n=11) of 100nM BAF and 500nM LEM2. Dotted lines, WLC model of λ-DNA. Linear fits (dashed lines) in the enthalpic regime (methods) reveal a stiffness but not a rest-length change between the two conditions (see main text). Red arrows illustrate tension increase ΔT when keeping DNA end-to-end distance fixed.

551 **e,** Effective stiffness as a function of LEM2 concentration (100nM BAF) measured via constant
552 tension experiments (Extended Data 4c, methods). Error bars, mean ± standard deviation; dashed
553 line, fit to the stiffening reinforcement model.

554 **f,** Sketch of the IDR-dependent mechanism of assembly-induced stiffening reinforcement. Top,
555 DNA, represented as a series of springs (stiffness k_o), is held in place at fixed end-to-end distance.
556 BAF-LEM2 module assembly results in the addition of springs in parallel (stiffness k_i). Saturated
557 BAF-LEM2 binding increases the effective stiffness of the system from K_0 (DNA alone) to $K_0 + K_i$.
558 Bottom, Saturated BAF-LEM2 binding and compliant element assembly generates tension T_{BAF-}
559 $_{LEM2}$ (magenta arrows) in addition to DNA tension T_{DNA} (yellow arrows), increasing the total
560 tension experienced by the system (pink arrows).

561

562

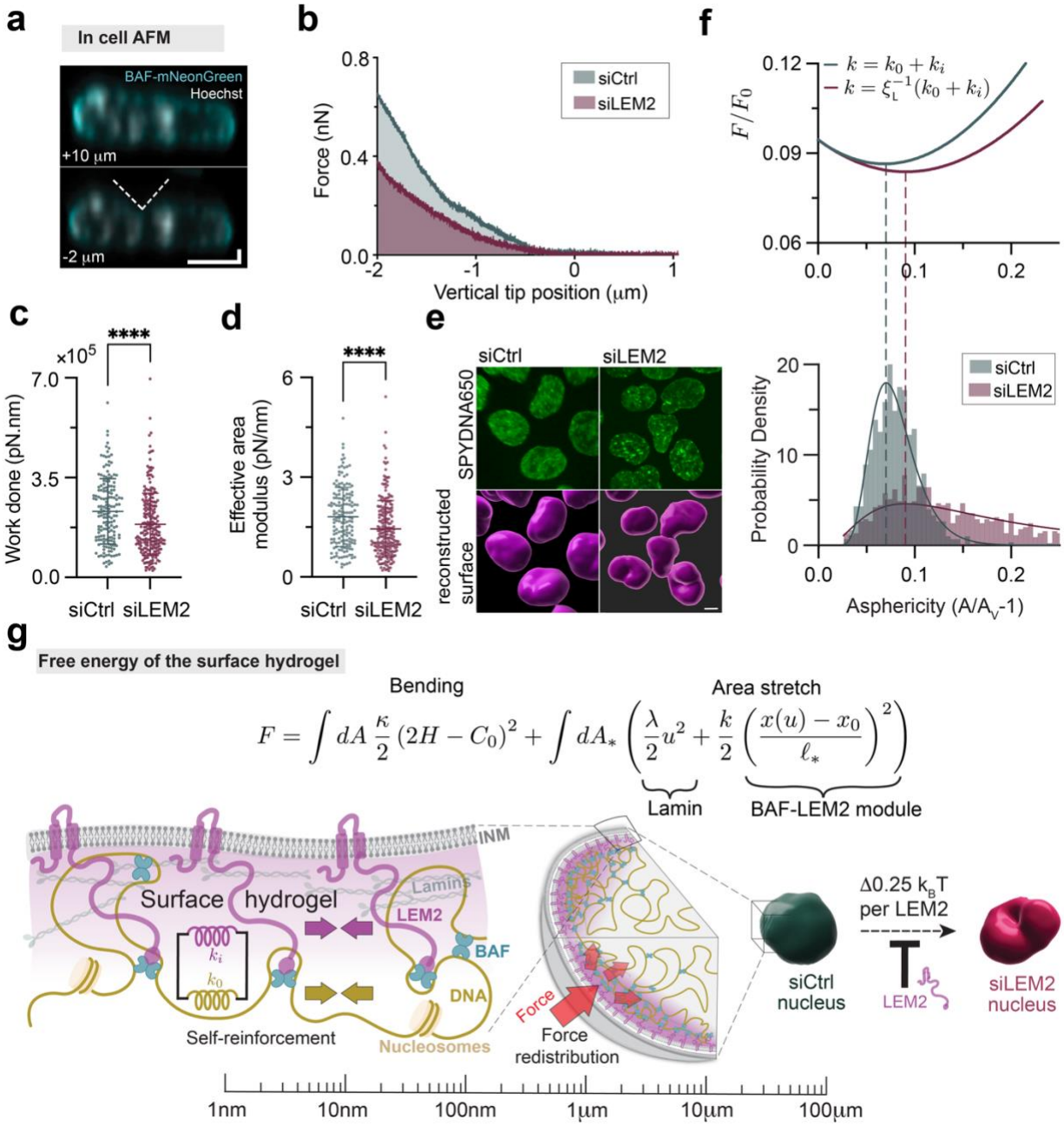

Fig. 3: A cross-linked network of LEM2-BAF-DNA forms a surface hydrogel that reinforces the nuclear periphery to regulate its morphology and integrity.

a, Representative live-cell images of AFM indentations of HCT-116 BAF-mNeonGreen cells; not indented (vertical tip position +10 µm) and indented (vertical tip position -2 µm). Dashed white line, illustration of pyramidal cantilever tip. Scale bar, 5 µm (horizontal and vertical).

b, Representative AFM force-indentation curves of nuclei of latrunculin A-treated HCT-116 cells, for siCtrl and siLEM2 cells. The cantilever makes contact with the nucleus at a vertical tip position

of 0 µm, and we measure the mechanical work (shaded areas under the curves) required to indent the nucleus by 2 µm. Indentation in absence of LEM2 requires less work than in presence. Segmentation of the nuclear surface reveals the nuclear surface area increase (Extended Data Fig. 10b), which together with the mechanical work (**c**) allows for determination of the effective area modulus shown in (**d**, methods).

c, Mechanical work for a 2 µm indentation of the nucleus of siCtrl and siBAF cells (methods), from three biological replicates (siCtrl: n = 159, siLEM2: n = 225).

d, Effective area modulus of nuclei of siCtrl and siLEM2 cells (Extended Data Fig. 10d; siCtrl: n = 159, siLEM2: n = 225, methods).

e, Top, confocal image stacks of DNA (SPYDNA650) of siCtrl (left) and siLEM2 (right) cells. Bottom, 3D segmentations of the nuclear surfaces for determining nuclear volume, shape, and surface area.

f, Top, plots of the normalized free energy (F/F_0) of the REMM model (methods) as a function of nuclear asphericity reveal that the minimum for the siLEM2 condition with $k = \xi_L^{-1}(k_0 + k_i)$ with measured stiffness ratio ξ_L (Supplementary Note 1) is placed at a larger asphericity than for the siCtrl condition with $k = k_0 + k_i$. Bottom, histograms of nuclear asphericity (measured as in **e** for siCtrl and siLEM2 cells (n = 603 and n = 901, respectively, pooled across three biological replicates). Colored lines, log-normal fit. With REMM model parameters $\lambda = 0.014$ pN/nm, $A_* = 1.8\, A_V$, $\kappa = 0$, rest length mismatch $x_0/x_* = 0.75$ and energy scale $F_0 = \lambda A_*$. The histograms peak at the values that minimize the corresponding REMM surface hydrogel free energy F (vertical dashed lines).

g, A nuclear surface hydrogel at the nuclear periphery. Top (theory), surface hydrogel free energy (F) is determined by integration over the strain-free area (A_*) of a bending energy term (left), with bending modulus κ and average and spontaneous curvatures H and C_0, a bare area elastic energy term (middle) representing lamins with bare elastic area modulus λ and surface strain u, and a DNA-BAF-LEM2 module term (right) with stiffness k, stretch relative to rest length $x(u) - x_0$ with $x(u) = x_*\sqrt{1+u}$ and $x_* = x(0)$, and surface density of DNA-BAF-LEM2 modules in the strain-free state $1/l_*^2$ (Supplementary Note 1).
Bottom left (sketch, molecular scale), schematic of the REMM surface hydrogel (purple shade) formed below the INM (gray), comprising LEM2 (magenta), BAF (cyan), DNA (yellow), lamin filaments (green) and nucleosomes, with reinforcing properties as described (elastic properties indicated by coloured springs, tension indicated by colored arrows). Bottom middle (sketch, mesoscale), the surface hydrogel acts as a mechanical buffer, redistributing force along the nuclear periphery to maintain structural integrity under load. Bottom right (sketch, cellular scale), nuclear morphology is regulated by the integrity of the surface hydrogel. LEM2 depletion weakens the cross-linked shell, leading to reduced mechanical resistance and increased nuclear asphericity (red) compared to the more spherical shape in control cells (green).

INM Proteins	Copy number	Average spacing (nm)
BAF dimers*	3.64×10^5	37
LEM2	8.20×10^4	79
Other LEM proteins	2.14×10^6	15
Lamin A/C	3.60×10^5	38
Lamin B dimers	1.71×10^6	17

608 **Table 1: Copy numbers and average spacing of INM proteins.** *Dimers confined only to the
609 nuclear surface (Extended Data Fig. 5i).